Small, Volume 15, Issue 49, 2019, Article number 1904422
DOI: 10.1002/smll.201904422

Controlling Homogenous Spherulitic Crystallization for High-Efficiency Planar Perovskite Solar Cells Fabricated under Ambient High-Humidity Conditions

Dechan Angmo, Xiaojin Peng, Aaron Seeber, Chuantian Zuo, Mei Gao, Qicheng Hou, Jian Yuan, Qi Zhang, Yi-Bing Cheng, and Doojin Vak**

Dr. D. Angmo, Dr. X. Peng, Dr. A. Seeber, Dr. C. Zuo, Dr. M. Gao, Dr. D. Vak
CSIRO, Manufacturing
Clayton, VIC 3168, Australia
E-mail: dechan.angmo@csiro.au; doojin.vak@csiro.au
Dr. X. Peng, Prof. J. Yuan, Prof. Q. Zhang
State Key Laboratory of Silicate Materials for Architectures
Wuhan University of Technology
Wuhan, 430070 Hubei, P. R. China
Dr. X. Peng, Prof. J. Yuan, Prof. Q. Zhang
Glass and Technology Research Institute of Shahe
Shahe, 054100 Hebei, P. R. China
Dr. Q. Hou, Prof. Y.-B. Cheng
Department of Chemical Engineering
Monash University
Victoria 3800, Australia
Prof. Q. Zhang
School of Aerospace, Transport and Manufacturing
Cranfield University
Cranfield, Bedfordshire MK43 0AL, UK
Prof. Y.-B. Cheng
State Key Laboratory of Advanced Technology for Materials Synthesis and Processing
Wuhan University of Technology
Wuhan, 430070 Hubei, China

Abstract
The influence of precursor solution properties, fabrication environment, and antisolvent properties on the microstructural evolution of perovskite films is reported. First, the impact of fabrication environment on the morphology of methyl ammonium lead iodide ($MAPbI_3$) perovskite films with various Lewis-base additives is reported. Second, the influence of antisolvent properties on perovskite film microstructure is investigated using antisolvents ranging from nonpolar heptane to highly polar water. This study shows an ambient environment that accelerates crystal growth at the expense of nucleation and introduces anisotropies in crystal morphology. The use of antisolvents enhances nucleation but also influences ambient moisture interaction with the precursor solution, resulting in different crystal morphology (shape, size, dispersity) in different antisolvents. Crystal morphology, in turn, dictates film quality. A homogenous spherulitic crystallization results in pinhole-free films with similar microstructure irrespective of processing environment. This study further demonstrates propyl acetate, an environmentally benign antisolvent, which can induce spherulitic crystallization under ambient environment (52% relative humidity, 25 °C). With this, planar perovskite solar cells with ≈17.78% stabilized power conversion efficiency are achieved. Finally, a simple precipitation test and in situ crystallization imaging under an optical microscope that can enable a facile a priori screening of antisolvents is shown.

1. Introduction

With certified power conversion efficiency (PCE) reaching 24%, perovskite solar cells (PSCs) already rival record PCE of commercial CdTe [1]. Beyond the proof-of-concept devices, the challenge now is to enable competitive cost-per-watt for PSCs to become commercially feasible. Toward this end, materials and processing should be streamlined for industry-compatible manufacture. A critical bottleneck in the state-of-the-art PSCs is the ubiquitous practice of PSC fabrication under inert nitrogen environment with trace amount oxygen and humidity levels achieved using a glovebox. In industrial manufacturing scenarios, operating large equipment under inert environment is costly as well as impractical. As a result, the PCE of cells fabricated through industry-compatible manufacture often lags compared to lab-based cells fabricated under an inert envi-ronment [2-5]. Although fabrication under ambient environment is touted as the reason for the reduced efficiency, how and why the environment imparts such dramatic changes in photovoltaic properties of PSCs is seldom, if at all, explored.

Ambient environment implies the presence of both humidity and oxygen. PSCs fabricated under a dry environment with relative humidity (RH) maintained at 20% have enabled high PCEs exceeding 20% [6], which is similar to inert-processed PSCs. On the other hand, PSCs fabricated in uncontrolled ambient environment where humidity is generally above 30% have resulted in significantly lower efficiencies.[7–10] As oxygen level is not regulated in these studies, one can infer that humidity is the main agent influencing the photovoltaic properties.

While water or humidity can affect PSCs during solution preparation, device fabrication, and device operation,[11,12] the impact of moisture during device fabrication remains the least understood due to the myriad fabrication methods, materials, and device structures used for PSCs.

Most studies on humidity effect during fabrication focus on the annealing step,[13–16] film fabrication via the two-step process,[8,9,16] and/or employ the mesoporous structure, with impressive efficiencies[6,16–19] There are a very few reports on one-step fabrication of PSCs in a planar device structure, a simpler and cost-effective method, which highly favorable for upscaling through roll-to-roll processing and especially suited for stable variants of perovskites such as the mixed halide compositions.[20,21] However, the planar structures are highly sensitive to defects such as pinholes in the film which can cause short-circuit in the device, compared to the mesoporous structure where the thick TiO2 layer prevents short circuits and helps in achieving uniform films by reducing evaporation. Additionally, the use of one-step process with planar structure introduces further difficulties in achieving uniform films over large area due to the strong ionic reactions between lead iodide and cations, which preferentially induce rapid crystal growth and suppresses nucleation, leading to poor surface coverage. On the other hand, the two-step process involves deposition of PbI2 and then conversion into perovskite by sequentially depositing organic cations. PbI2 films used in two-step process tend to form highly compact uniform films. Most strategies thus focus on making PbI2 film porous to enhance infiltration of organic cations and achieve complete conversion of PbI2 into perovskites. Thus, strategies generally employed for mesoporous structure and two-step processing in ambient or inert conditions do not work for one-step planar devices fabricated in ambient conditions.

With these difficulties, it is no surprise that a very few reports deal with the ambient fabrication of perovskite films through one-step process in a planar devices and efficiencies are generally poorer than for two-step or mesoporous devices. Watson et al. demonstrated the fabrication of perovskites using ethyl acetate as an antisolvent and reported a PCE of 14.5–15% in planar devices fabricated in ambient high-humidity environment. By studying the solubility of water in the antisolvent, Watson et al. proposed moisture sequestering of antisolvent as a key parameter [22]. Cheng et al. employed one-step fabrication under different environment and achieved a PCE of 5% under high humidity with MAPbI3.[23] At the time of submitting this manuscript, few other reports emerged on the ambient processing of planar n–i–p devices with high efficiencies, however these devices make use of materials such as Spiro-MeoTAD and gold that are not feasible for commercial prospects of PSCs from stability as well as cost perspective[24].

Irrespective of these complexities in device structures and fabrication methods, most studies base their analyses on the microstructure of perovskite films as a bottom-line relating macroscopic electrical or mechanical property on grain size, shape, mutual distribution, structure, orientation, and chemical composition. It is therefore important to understand the underlying mechanism in microstructural evolution to device strategies to modulate microstructure and the resulting properties, for example, to tackle challenges with poor film coverage and pinholes or to induce certain crystallographic phases and orientations. The evolution of microstructure in perovskite films is driven by crystallization. Crystallization undergoes two steps, nucleation and crystal growth. Supersaturation provides the driving force for crystallization, which is attained on exceeding the saturated equilibrium concentration of solute. The degree of supersaturation can be increased by increasing the solute concentration, increasing solvent evaporation or decreasing the solute solubility or a combination thereof. Practically, these involve the use of temperature change, anti-solvents addition, pH change, pressure change, etc. Various kinetic factors (for example, supersaturation, ion mobility, conformation freedom, etc.) and thermodynamic factors (for example, solubility, solid–liquid interfacial tension, solvent activity, temperature, etc.) determine the rate and mechanisms by which crystals are formed from solutions.[25] These kinetic and thermodynamic factors are influenced by both bulk physical properties (for example, viscosity, vapor pressure, surface tension, etc.) and molecular properties (such as hydrogen bonds, noncovalent bonds, molecular networks, etc.).[26] While many of these crystallization strategies are employed in perovskite film fabrication such as nitrogen blowing during deposition,[27] antisolvent treatment,[28–31] deposition on heated substrates,[32,33] adding acids and bases in the precursor ink,[34] or a combination thereof,[17,35] the mechanism by which these strategies induce the changes observed in microstructure are seldom thoroughly investigated.

Among the various crystallization techniques, the antisol-vent approach is arguably the most popular method in perov-skite film fabrication. First proposed simultaneously by Spiccia et al.[28] and Seok et al.,[36] the method involves dropping of an antisolvent at a critical stage during the spin-coating process, which enables the formation of uniform films with large-grains. Xiao et al. explored a series of solvents and proposed the dropping of an antisolvent will reduce the solubility of the perovskite in the mixed solvent, thereby promoting fast nucleation and growth. Since then, the antisolvents demonstrated in these studies, chlorobenzene (CB) and toluene (Tol), have been universally adopted with processing carried out under inert environment leading to record efficiencies.[29,30,37] However, these solvents form nonuniform porous films under ambient processing environments.

Thus, we aimed to understand how device fabrication in an ambient environment impact microstructure evolution of perovskite films when processed through one-step method and how antisolvents interact with ambient moisture and perovskite precursors to regulate perovskite microstructural evolution. Initially, we evaluated the impact of commonly used precursor additivities, namely, dimethyl sulfoxide (DMSO), N-methyl-2-pyrrolidone (NMP), and ɤ-butyrolactone (GBL) on the morphology of perovskite films in ambient and inert conditions. We then systematically investigated perovskite film formation using antisolvents having a wide range of polarity to understand the interaction of antisolvent and the precursor solution. In situ crystallization imaging using an optical microscope and a simple precipitation test unveils a wealth of information about the interaction of antisolvents with precursor ions and environment conditions. To further establish the best film forming conditions, we fabricated p–i–n type inverted planar PSCs in the ambient environment (52% RH) where all but the electrodes were solution-processed and only two low-temperature (<140 ºC) drying steps were employed. We report a stabilized efficiency exceeding 17.78%—the highest reported to date for an ambient-processed p–i–n planar device fabricated with the antisolvent method.

2. Results and Discussion

First, we compared the influence of inert and ambient environment on the film formation upon deposition of perovskite precursor solution without antisolvent treatment (Figure S1, Supporting Information). The precursor solution comprised MAI:PbI2 mixed in 1:1 molar ratio in 600 mg of N,N-dimethyl-formamide (DMF). We further studied the influence of processing environment on the film morphology upon the addition of DMSO, NMP, and GBL in equimolar ratio to the MAI and PbI2 in the DMF solution, following the procedure reported by Park et al.[31] We note that significant prior literature exist on the crystallization of perovskite precursors as well as on the interaction of precursor ions with different solvents in controlling crystallization.[38–40] Our goal of studying the film formation of precursor solution with and without different solvent additives is to focus on the differences between the films processed under ambient and inert environment. Irrespective of the presence of additives, we find that (1) ambient environment inhibits nucleation promoting crystal growth in comparison to inert processing environment; (2) ambient environment induces ani-sotropies in crystal growth. The presence of sharp needle-like crystal morphology in "wheat-sheave" like crystals signal the presence of large kinetic and interfacial free-energy anisotro-pies.[41] Such anisotropies are absent in inert-processed films. A detail discussion is given in the Supporting Information.

While none of the precursor solution type leads to complete surface coverage, round albeit sparse spherulitic islands emerge in DMF:NMP-based perovskite films processed under inert environment. Such spherulitic growth occurs when precursor ions experience an improvement in the rotational-to-translational ratio.[41] We later find evidence of such spherulitic growth as the underlying mechanism behind uniform film formation with the best

antisolvent system under ambient environment processing. Similar spherulitic crystallization, albeit much larger in size, is also observed in when perovskite inks are deposited on hot-substrates.[33,42,43]

What causes the anisotropies in perovskite crystal growth under an ambient processing environment? In the precursor solution, the DMF solvent, the additives DMSO and NMP, as well as I^- are Lewis bases, which can donate a lone pair to Lewis acids Pb^{2+} and MA^+ forming adducts MAI·PbI2·X, where X is DMF, NMP, or DMSO.[31,44] The adduct formation is also discernable during the spin-coating process when the yellow precursor film turns colorless.[31,45] Annealing at elevated temperature releases the intercalated additive forming a stable perovskite phase.[31] We observe that the transparent adduct phases heterogeneously converts to brown upon exposure to air starting from the film edges and surface. The strength of the adduct determines the rate at which the transition from the colorless adduct phase to the opaque brown perovskite phase takes place. Similar to our observation, others have reported that the colorless needle-like crystal of PbI2·DMSO adduct returns to original yellow color upon prolonged exposure to air.[45] Based on these observations, we propose that water molecules present in the atmosphere sequester the Lewis base DMSO/DMF/NMP from the adduct, which causes heterogeneity during nucleation and crystal growth and eventually leads to anisotropic crystal growth. This mechanism is likely because water has stronger bond affinity to DMF, DMSO, and NMP, respectively, than to itself, resulting in a complex formation.[46–50] As perovskite structure is held together by weak hydrogen bonding, even weaker bonding is to be expected in the metastable adduct phase, which would make the Lewis bases highly labile to sequestering by water.[51,52] Figure S2 of the Supporting Information illustrates the proposed mechanism, which is an extension of a previously proposed mechanism of intermolecular exchange of Lewis bases in adduct by organic cation.[53,54]

Figure S2 of the Supporting Information assumes that perfect octahedral PbI6 cages are formed, which may not be the case. Before the formation of the adduct phase, the coordination chemistry of the precursor with different additive is also likely to be different. Different solvent species are reported to compete with iodide ions for coordination with lead, which can result in different complexes.[40] Additionally, water is also likely to be absorbed in the precursor solution during deposition. Anta et al. observed that water molecules are retained in the perovskite films and coordinate with the Pb atoms as water is a stronger Lewis base than I^- ions.[55] Thus, anisotropy could also arise prior to the formation of the adducts. Further theoretical molecular dynamics and solution chemistry studies are needed to understand how and to what extent water is adsorbed during fabrication prior to adduct formation and how they interfere with the coordination chemistry of perovskite precursors.

2.1 Antisolvents under ambient processing environment

The morphology of the films without antisolvent suggested that a process is needed to increase the degree of supersaturation to enable greater surface coverage. Additionally, the process should not only retard crystal growth and promote nucleation but should also tackle the moisture-induced crystal-growth anisotropy under ambient conditions, encouraging homogenous spherulitic growth.

The antisolvent method is arguably the most utilized approach in laboratory-scale perovskite thin film fabrication to increase the degree of supersaturation.[28–31] We thus explored the potential of antisolvents for ambient fabrication. In this method, the precursor solution is spun on a rotating substrate. At an optimized timing, an antisolvent is dropped during the spin-coating. The wet film is then annealed to generate thin solid films. **Figure 1**a,b depicts the method and the underlying mechanism of film formation, respectively. As the antisolvent method is a common technique for growing nano-particles especially for pharmaceutical products, the crystallization mechanism is well-studied.[25] By selecting antisolvent in which precursor ions have poorer solubility than the parent solvent, rapid supersaturation is induced upon casting of the antisolvent, facilitating nucleation and crystal growth. Film formation occurs by agglomeration of crystals which subsequently undergoes densification/coarsening through grain boundary movement and Oswald ripening when a low temperature annealing step is applied.

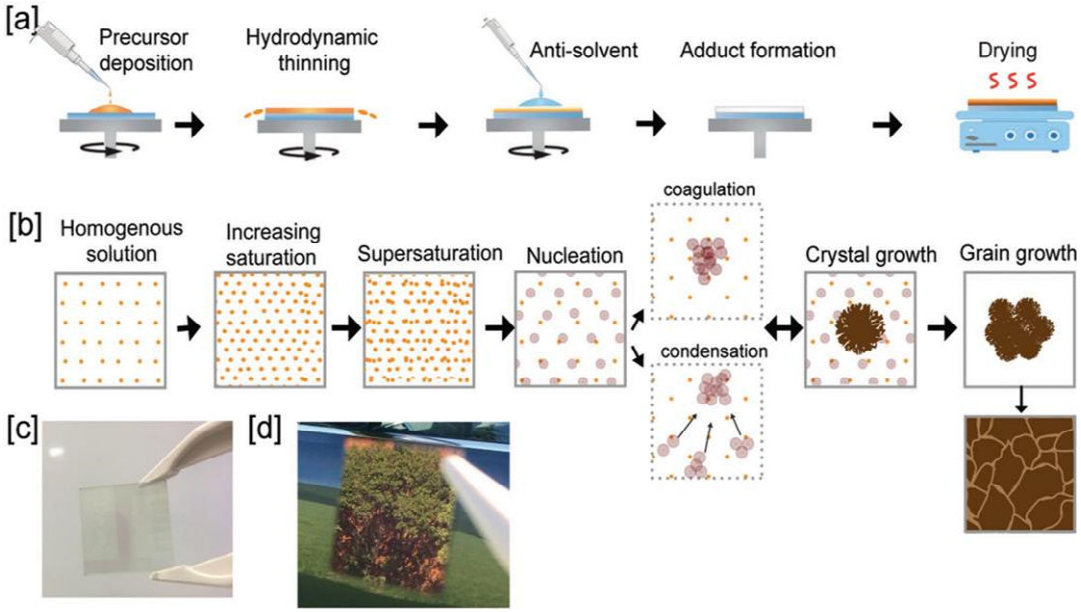

Figure 1. Schematics of a) the antisolvent method used in perovskite film fabrication and b) the underlying mechanism. c) A picture of the transparent adduct and d) a picture showing highly reflective film formed after annealing the transparent adduct. Schematics in (b) is adapted with permission.[25] Copyright 2012, Elsevier.

To understand how antisolvent interacts with precursor ions and the processing environment, we selected a range of anti-solvents initially based on their polarity: from apolar heptane to highly polar water as listed in **Table 1**. We used the precursor solution with PbI2:MAI:DMSO (1:1:1 molar ratio) in DMF. DMSO was used instead of NMP because of its compatibility with industrial processes due to its lower toxicity. The best films produced a transparent film upon deposition of antisol-vent, the indication of adduct formation, which became highly reflective upon drying at 100 ℃ for 2 min (Figure 1c,d). Both the bulk physical and chemical properties of the antisolvents affect crystallization. Various parameters such a boiling point, surface tension, dielectric constant, viscosity, vapor pressure, etc. describe bulk physical properties. However, less definitive parameters exist to describe chemical properties. We considered a range of such molecular descriptors including Heidelberg polarity parameter, and Hansen's solubility parameters but found hydrogen bond donor (α) and acceptor (β) propensity and dipolar–polarizability [π] descriptors are best at describing most of the observations.[56–59] These three descriptors represent a scale for quantifying van der Waals force (π) and hydrogen bonding (α, β) which primarily dictates solute–solvent and sol-vent–solvent molecular interactions. Table 1 lists the antisol-vents studied along with some key bulk physical properties and the chemical descriptors.

The discussion hereafter refers to two experiments: precipitation, and in situ crystallization. In the precipitation experiment, we introduced a fixed quantity of precursor solution into a vial containing the antisolvent. This simple test illustrates the interaction of antisolvents with the perovskite solution. In the in situ crystallization experiment, we injected a small fixed quantity of precursor solution into a set quantity of antisolvent and captured the ensuing crystallization using an optical microscope. Videos from both experiments are given the Supporting Information.

2.1.1 Nonpolar Antisolvent

The microstructure of nonpolar heptane-treated (HEP) perov-skite film resemble the ambient films without any antisol-vent treatment, henceforth referred as the control sample (**Figure 2**a). XRD patterns of HEP exhibit similar peaks as the control sample (Figure 2b). The major peaks at 14.10□, 23.47□, 24.48□, 28.11□, and 28.42□ correspond to (110), (211), (202), (004), and (220) planes, respectively, while the minor peaks at 19.90□, 19.98□, and 31.84□ correspond to (112), (220), and (310) planes, respectively of the tetragonal phase perovskite (space group *l4cm*). The diffraction peaks are narrow which suggest long-range crystalline domains. Particularly, the high intensity and narrow diffraction peaks of the (110) and (220) planes suggest strong orientation of crystallites along the long axis parallel to the substrate.[60–62] Crystallite sizes are also the same in both HEP and control samples (**Table 2**). Thus, HEP does not interact with the perovskite precursors.

The noninteraction of HEP in the perovskite film formation is because HEP is hydrophobic and nonmiscible to water, DMF, or DMSO. As dipole moment, hydrogen bonding propensities, and dispersibility are effectively zero, HEP also does not chemically interact with the perovskite precursors or with the water molecules (Table 1). The precipitation experiment and the in situ imaging conclusively confirm the lack of interaction as HEP and perovskite solution segregates like oil and water (Figure 2c,d; Video S1, Supporting Information). Additionally, HEP has very low dynamic viscosity and low vapor pressure, which further undermines any physical interaction (pressure felt by the perovskite precursors) such as interfering with the flow behavior of the solution or influencing evaporation rate of DMF during spin-coating. Thus, the wheat-sheave crystal structure forming incomplete surface coverage, as observed in the control sample, also appears in the HEP sample (Figure 2).

2.1.2. Polar Aprotic Antisolvents

We investigated several polar aprotic solvents. In ascending order of dipole moment, they are Tol, diethyl ether (DE), CB, tetrahydrofuran (THF), isopropyl acetate (IPAC), ethyl acetate (EAC), and propyl acetate (PAC). CB, THF, IPAC, EAC, and PAC can be considered borderline polar aprotic solvents because of their high dipole moment (□1.5 D), which is similar to the polar protic solvents such as IPA (1.56 D) (Table 1). The SEM images show all polar aprotic antisolvents result in films with significantly higher surface coverage than the control samples (**Figure 3**a). This observation shows that all polar-aprotic antisolvents interact with the such as Tol is sufficient to interact with precursor solution to retard

crystal growth and promote nucleation. The precipitation experiment clearly shows that even a slightly polar antisolvent precursor solution, inducing precipitation of the precursor ions (**Figure 4**; Video S1, Supporting Information).

Table 1. Physical and chemical properties of the solvent employed in this study.

	Structure	$\sum\alpha$[a]	$\sum\beta$[b]	π[c]	Dipole moment[d,e] [D]	Dielectric constant[e]	Boiling point[e] [°C]	Viscosity[e] [mPa s]	Surface tension[e] [dyn cm^{-1}]	Vapor pressure[e] [Torr]
Heptane		0	0	−0.08	0	1.91	98	0.39	28.28	36
Toluene		0	0.14	0.54	0.38	2.37	132	0.56	40.2	29
Diethyl ether	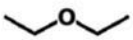	0	0.41	0.27	1.15	4.24	35	0.22	23.96	442
Chlorobenzene	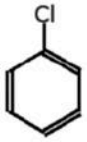	0	0.07	0.71	1.69	5.7	111	0.75	47.48	9
Tetrahydrofuran		0	0.48	0.58	1.75	7.43	66	0.46	39.44	142
Ethyl acetate	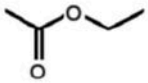	0	0.45	0.55	1.78	5.99	77	0.42	33.67	73
Propyl acetate	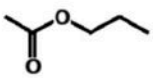	0	0.45	0.5	1.80	5.52	102	0.54	34.26	25
Isopropyl acetate[f]	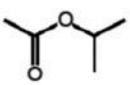	–	–	–	1.75		89	0.46	22.1	47
Isopropyl alchohol	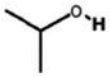	0.33	0.56	0.48	1.56	19.26	82	2.04	30.13	32
Water	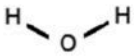	1.17	0.47	1.09	1.87	78.36	100	0.89	104.7	23.76
N,*N*-dimethylformamide	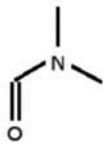	0	0.74	0.88	3.82	37.22	153	0.79	49.56	3.8
Dimethyl sulfoxide	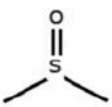	0	0.88	1	3.96	46.83	189	1.99	61.78	1
N-methyl-2-pyrrolidone	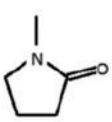	0	0.77	0.92	4.10	32.2	202	1.67	58.58	0

[a]$\sum\alpha$ is the sum of hydrogen bond donor propensity[56–59]; [b]$\sum\beta$ is the sum of hydrogen bond acceptor propensity[56–59]; [c]π Polarity/polarizability of solvent[63–66]; [d]Data collected from online databases PubChem and NIST; [e]Refs. [63–66]; f) Data not available.

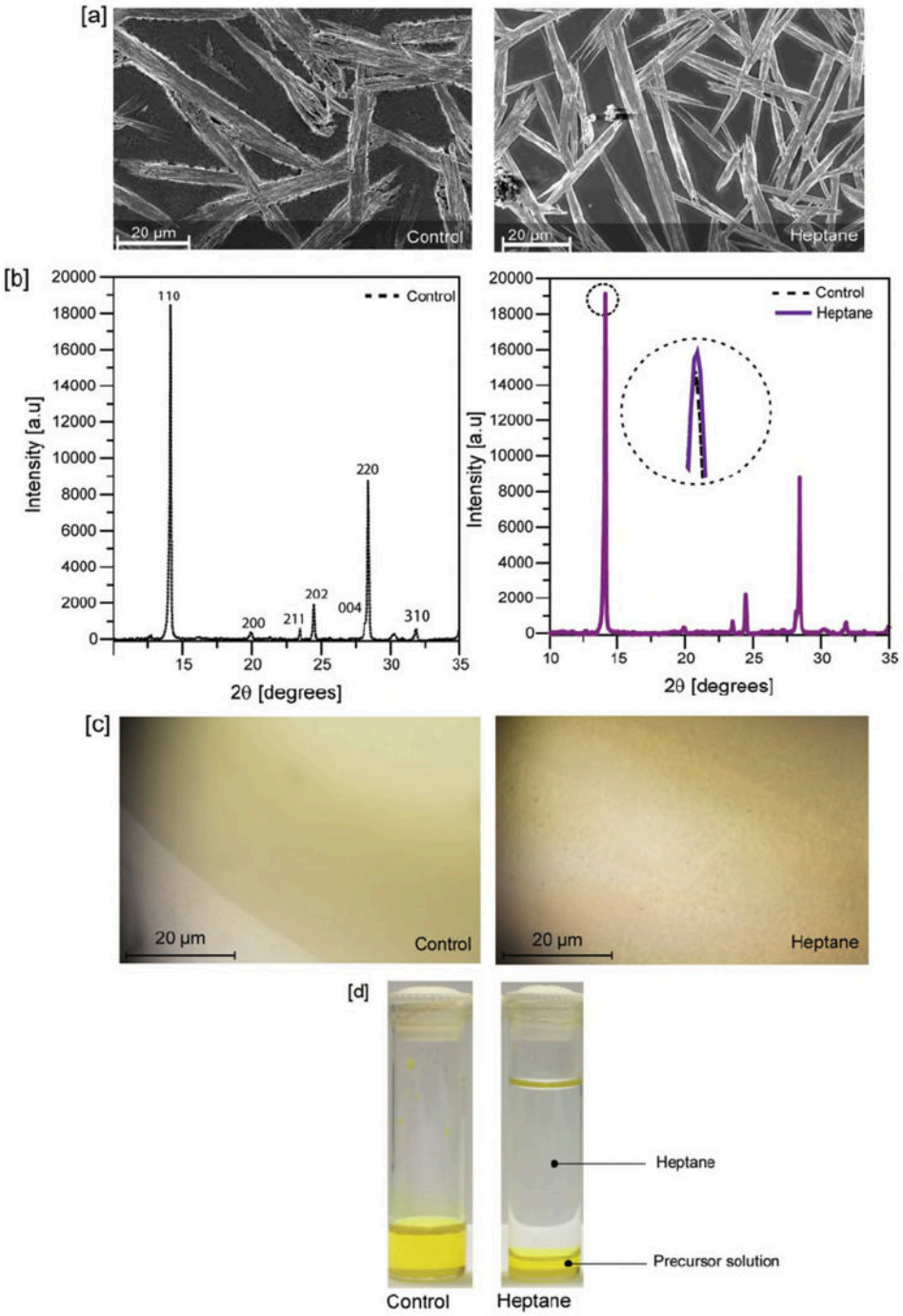

Figure 2. a) SEM images of perovskite films fabricated under ambient (room) environment without any antisolvents treatment (control) and with nonpolar antisolvent (heptane) treatment. b) XRD pattern of the control and heptane-treated perovskite films. c) Images of precursor solution and precursor ink in heptane captured during the in situ crystallization imaging (Video S2, Supporting Information). d) A picture of the vial after the precipitation test of precursor solution in heptane. Control is simply the precursor solution.

Table 2. Lattice parameters and crystallite size extracted from XRD data of perovskite films treated with different antisolvents. All are ambient processed, except otherwise stated.

Sample info	*a* parameter [Å]	*c* parameter [Å]	Crystallite size [nm]
Control (no antisolvent)	8.873 ± 0.001	12.661 ± 0.001	230 ± 10
Heptane (HEP)	8.872 ± 0.001	12.661 ± 0.001	234 ± 12
Toluene (Tol)	8.8717 ± 0.0005	12.653 ± 0.002	199 ± 9
Diethyl ether (DE)	8.871 ± 0.001	12.657 ± 0.002	208 ± 14
Chlorobenzene (CB)	8.8713 ± 0.0005	12.656 ± 0.002	137 ± 4
Ethyl acetate (EAC)	8.8706 ± 0.0005	12.654 ± 0.003	132 ± 5
Propyl acetate (PAC)	8.8755 ± 0.0005	12.662 ± 0.002	173 ± 9
Isopropyl acetate (IPAC)	8.8712 ± 0.0006	12.659 ± 0.001	154 ± 7
Isopropyl alchohol (IPA)	8.869 ± 0.001	12.655 ± 0.003	120 ± 7
Tetrahydrofuren (THF)	8.868 ± 0.002	12.652 ± 0.006	105 ± 9
TOL (inert)	8.8719 ± 0.0005	12.659 ± 0.002	138 ± 5
CB (inert)	8.8724 ± 0.0005	12.660 ± 0.002	147 ± 6
PAC (inert)	8.8717 ± 0.0005	12.653 ± 0.002	137 ± 5

XRD patterns highlight improved surface coverage with the use of apolar protic anti-solvents. The diffraction intensities of the (110), (202), and (220) planes decreases with polar aprotic antisolvents treatment while the intensities of (200), (211), and (310) planes increases (Figure 3b,c). To elucidate this further, integrated intensity of a peak or peak area is a more reliable parameter than absolute peak intensity. Figure 3d contains a bar graph of the peak area of the three main peaks (110), (220), and (310), each is normalized to the corresponding peak area of the control sample. This graph highlights (310) plane rapidly evolves with the use of polar aprotic antisolvents in comparison to the control. However, the evolution of the (310) plane does not directly correspond to growth retardation of the (110) plane. Figure 3e highlights the relative retardation of (110) plane with the use of different antisolvents. This graph shows that growth retardation occurs in all but CB-treated film. Thus, surface coverage improvement with polar aprotic solvent treatment fabricated in air occurs by reorientation of crystallites in addition to increasing nucleation/retarding growth.

While the polar aprotic antisolvents lead to significantly improvement surface coverage in compared to the control sample, stark differences exist in films processed with different antisolvents (Figure 3a). Tol and CB lead to porous films whereas DE, ETAC, PAC, and IPAC lead to compact films with larger grains with an average diameter ≈100–200 nm. THF shows a very different morphology, which comprises of small grains interspersed with small pores. Tol, DE, and CB have similar poor water solubility (≈0.5 g L^{-1}), which suggests water sequestering by the antisolvent is not the primary factor dictating microstructure evolution, as has been previously proposed.[22] The morphology trend also does not follow the polarity trend. The discussions hereafter present different subheading dedicated to individual or group of polar aprotic antisolvents to distinguish the underlying differences in micro-structural evolution with different polar aprotic solvents.

DE: Among all other polar aprotic solvents studied here, DMSO is immiscible to only DE. This immiscibility preserves the precursor adduct with DMSO when DE is introduced during spin-coating. As observed from the DMF:DMSO sample without antisolvent treatment (Figure 1), retaining DMSO should induce higher nucleation and suppress crystal growth to a larger extent than by the use other antisolvents in which both DMF and DMSO are miscible. XRD pattern of the DE-treated film confirm the enhancement of nucleation and suppression of crystal growth. (110) peak area decreases by over 50% compared to the control, which is the second highest reduction compared to most other polar

aprotic solvents, indication crystal growth retardation (Figure 3e). At the same time, (310) peak area in DE-treated films increases by 200% compared to the control, which indicates strong reorientation of the crystallites and high probability of increased nucleation (Figure 3d).

In addition to the preservation of the adduct, DE further contributes toward a higher degree of supersaturation during spin-coating by increasing the evaporation rate of DMF due to its higher vapor pressure and low surface tension compared to DMF. In situ crystallization imaging shows sparse nucleation, but spontaneous crystal growth is not detected in DE unlike the other antisolvents (Figure 4a; Video S2, Supporting Information) as DE rapidly volatizes. However, rapid formation of precipitate in DE in the precipitation test confirms increased nucleation and crystal growth in DE.

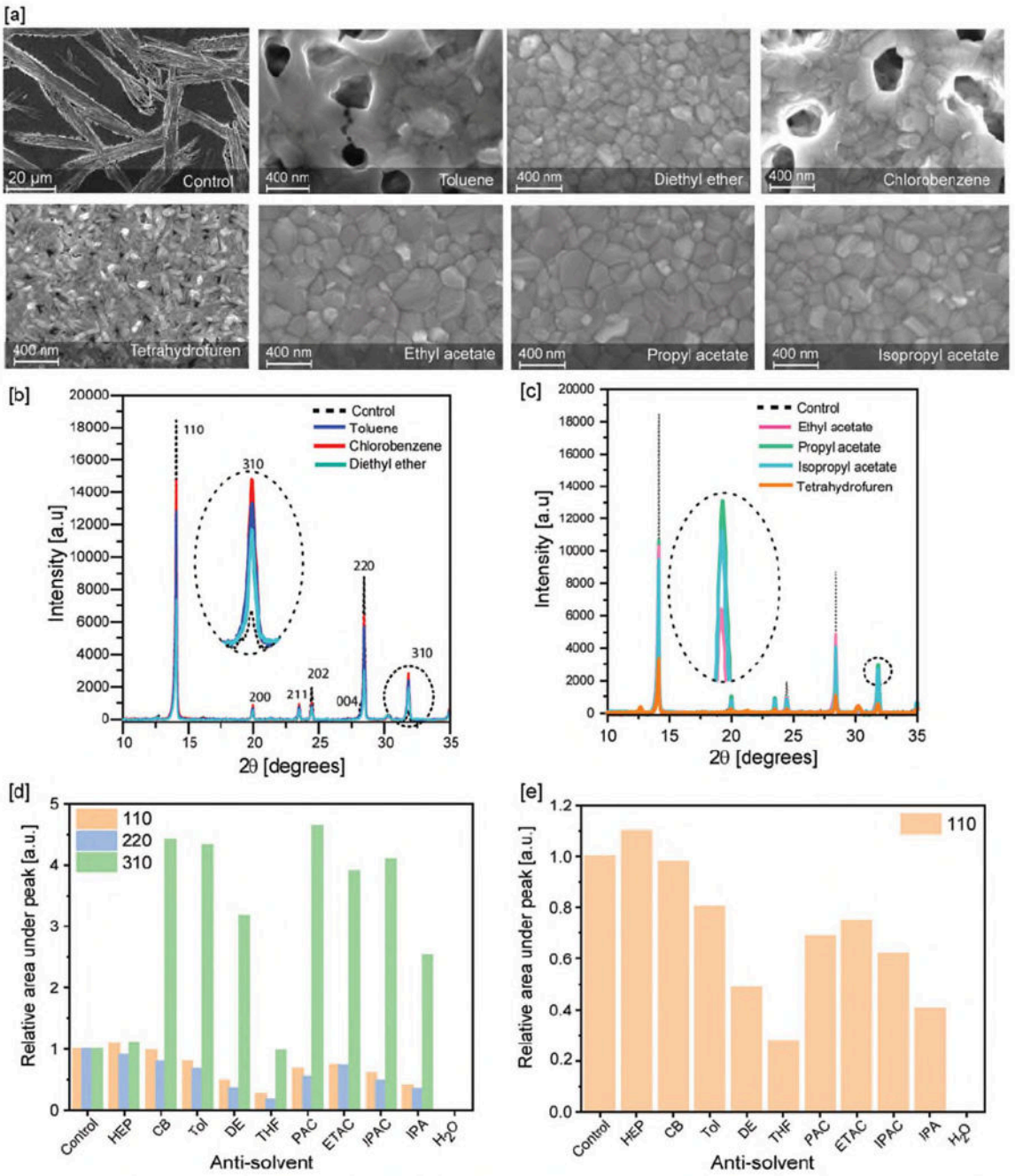

Figure 3. a) SEM images of perovskite films fabricated under ambient environment with different polar aprotic antisolvents. b,c) XRD patterns of perovskite films fabricated under ambient environment with different polar aprotic antisolvents. (c) The effect of different antisolvents on the evolution of different crystallographic planes. The peak area of three main crystallographic planes (110, 220, and 310) is normalized with respective peak area of the control sample. d) The effect of antisolvents on the evolution of the (110) plane normalized to the corresponding peak of the control sample.

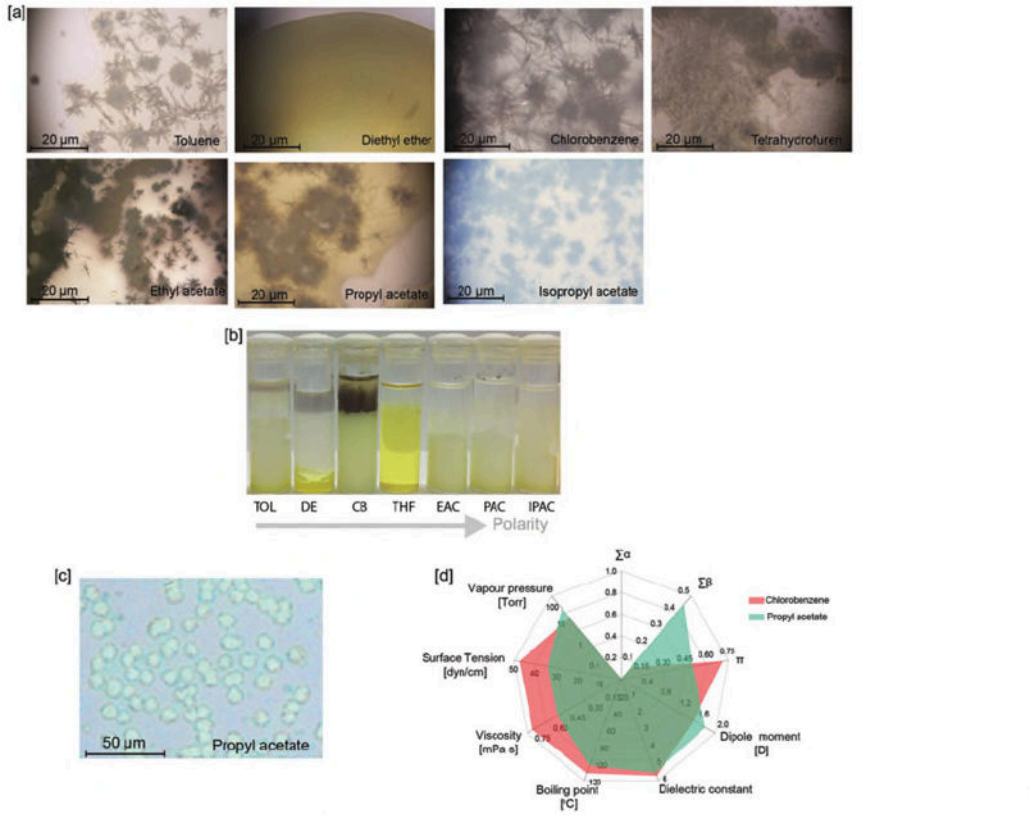

Figure 4. a) Frames captured during the in situ crystallization imaging of perovskite precursor in different polar aprotic antisolvents in ambient environment (Video S2, Supporting Information). b) Images after precipitation of precursor solution in different antisolvents in ambient environment. c) The optical image shows spherulitic islands emerge as the transparent adduct film fabricated in ambient environment with propyl acetate treatment is monitored over time. d) A radar plot comparing the properties of chlorobenzene and propyl acetate.

CB and Tot: CB and Tol lead to higher surface coverage than the control but pores are present in both films. Unlike DE, DMSO and DMF are miscible in CB and Tol. Thus, dropping of these antisolvents destroys the adduct, undermining the effect of adduct on crystal growth retardation/nucleation enhancement. The (110) peak area of CB-treated film is similar to the control sample, however the crystallite preferential orientation in the (310) plane is over 300% higher in CB-treated film compared to the control film. These results indicate that CB treatment do not impede crystal growth rate, however, it effects preferential orientation of crystallites.

On the other hand, Tol-treated film demonstrate 20% reduction in the peak area of the (110) plane compared to control or CB. At the same time, the Tol-treated film shows higher preferential orientation in the (310) plane compare to CB-treated films. These results show Tol also retard crystal growth while also inducing nucleation of new crystallites. The calculated crystallite size further confirms the nonretardation of growth rate in CB, which leads to larger crystallite size (199 nm) in comparison with Tol (137 nm). In situ microscopy imaging further show spontaneous crystallization occurs in both Tol and CB and crystals grow to larger size in CB than in Tol. In situ microscopy further shows heterogeneous crystallization in both CB and Tol manifests as distinct perovskite crystal habits in both these antisolvents (Figure 4a; Video S2, Supporting Information). Tol samples exhibit a mix of columnar structures, spherulites with broad columnar branches as well as needle-like branches. On the other hand, CB sample comprises of needles, spherulites with fine needle-like branches extending to different lengths, and wheat-sheave crystal structures reminiscent of the microstructure of control sample in ambient conditions albeit with significantly reduced length. This inhomogeneity in the crystallization ultimately result in porous morphology due to nonuniform densification upon annealing.[63]

The differences between CB and Tol samples could shed light on to the differentiation mechanism between growth retardation and crystallite reorientation. As observed in control samples, moisture

facilitates crystal growth (Figure 1). Thus, the nonretardation of crystal growth with CB treatment indicates that CB offers poorer defense against moisture. The precipitation experiment further supports this hypothesis as rapid browning at the precursor/air interface is observed, which is more severe in CB than Tol (Figure 4b; Video S1, Supporting Information). CB has the highest dipole moment, viscosity, and surface tension but the poorest hydrogen bond donor propensity among all polar aprotic solvents (Table 1). Thus, CB is unlikely to form any strong hydrogen bonds with the moisture in the environment, the precursor ions, or the solvent molecules. Hence, CB leaves the precursor ions susceptible to moisture in the environment, which induces the higher degree of browning or heterogeneous crystallization as observed in the CB/precursor mixture in the precipitation experiment. This poor defense against moisture lead to the crystallite size in CB samples being larger than Tol samples, despite the higher surface tension and viscosity CB than Tol, which should otherwise facilitate higher nucleation and lower crystallite size.[64] Supporting evidence can be observed in the crystallite size which is significantly higher for ambient-processed CB sample than inert-processed CB sample. To further confirm the impact of hydrogen bond acceptor propensity being a critical parameter for defense against moisture, we conducted the precipitation experiment in the glovebox. Browning at the liquid/air interface did not occur in Tol under our solvent glovebox with 5% RH, which confirms that moisture indeed causes the heterogeneity and that hydrogen bonding propensity may be crucial at tackling moisture induced heterogeneity in crystallization. However, CB showed rapid browning in the inert environment similar to the ambient environment. We believe that this is due to the extremely poor hydrogen bonding propensity of CB, which cannot tackle even a slight amount of moisture.

Esters-Based Antisolvents: All ester group antisolvents, EAC, PAC, and IPAC, form uniform films with no porosity, comprising larger grains compared to all other antisolvents studied here. Precipitation experiment reveals uniform precipitation without any heterogeneous browning at the liquid/air interface (Figure 4b). Thus, the ester-based solvents induce uniform supersaturation, which promotes homogenous nucleation and crystal growth. The in situ crystallization imaging confirms uniform and homogenous multidimensional spherulitic crystal formation leading to increased space-filling, which ultimately translates to pinhole-free microstructure with larger grains compared to all other antisolvents (Figure 4a; Video, Supporting Information). We note that the radially distributed needles only originate in the crystallization imaging while supersaturation depletes as crystal growth proceeds; but they indicate formation of spherulitic islands similar to ones observed in the NMP sample under inert environment (Figure 1). Figure 4c shows spherulitic islands emerge over time in the transparent phase adduct in films treated with the ester-based antisolvents.

The presence of spherulites indicate ions movement to the interface of propagation is slowed down and reorientation of the ions relative to the propagating interface has occurred, enabling low-angle branching.[41,65,66] The ester-based solvents are also aprotic like CB and Tol. However, they exhibit significantly higher hydrogen bond acceptor propensities than Tol and CB.Thus, these solvents are likely to reinforce solvation of the ions by forming stronger hydrogen bonds than CB or Tol. Additionally, the hydrogen bond acceptor propensities of esters are similar to water which mean they can effectively shield the precursor ions from moisture in the environment. The shielding from moisture is further evident in the precipitation experiment where partial browning at the liquid/air interface does not occur in ester-based antisolvents compared to antisol-vents with lower hydrogen bonding propensities such as CB and Tol.

The comparison of CB and PAC further substantiates the key role of hydrogen bonding parameter. Both are polar aprotic solvents and DMF and DMSO are miscible in both solvents. Figure 4d shows a radar plot comparing all parameters from Table 1 of CB and PAC, which shows all parameters of PAC is lower or comparable to CB except hydrogen bond acceptor propensity. The hydrogen-bond acceptor propensity in CB is negligible (0.08), whereas it is five times higher in PAC (Table 2). CB treatment leads to marginal decline (2%) in the peak area of the (110) plane compared to the control whereas PAC treatment leads to significant decline (32%) in the (110) plane, which indicates stronger retardation of crystal growth with PAC treatment than with CB-treatment (Figure 3e). Additionally, PAC-treated films show the highest peak area of the (310) plane among all samples, which shows superior reorientation of crystallites and indicates increased propensity toward uniform spherulitic crystal growth.

THF: THF displays an anomaly compared to all other anti-solvents. The precursor solution does not precipitate but disperses in THF, which is likely caused by the molecular repulsion between THF and DMF.[67] As a result, crystal growth is stunted with THF treatment, which leads to the smallest grain size

as well as smallest crystallite size for THF-treated films samples (Figure 3a and Table 2). In situ crystallization imaging shows THF induces sparse and heterogeneous crystal growth as the solvent evaporates (Figure 4a; Video S2, Supporting Information). Crystal growth occurs in the shape of large needles and occasionally spherulites confined to the coffee-ring perimeter where local concentration of precursor is high.

2.1.3. Polar Protic Antisolvent

Water (H2O): By contrast to nonpolar HEP, highly polar H2O treatment leaves behind a yellow film resembling PbI_2. The precipitation experiment also shows the formation of a yellow precipitate (**Figure 5**a; Video S1, Supporting Information). In situ microscopy shows distinct rapid crystallization leading to nanocrystal agglomerates, which is a preceding process leading to PbI_2 polyhedral crystals growth[68] (Figure 5c; Video S2, Supporting Information). The nanocrystals veritably convert to polyhedral PbI_2 platelets upon annealing as evident in the SEM image and confirmed by the XRD (Figure 5b–d).

The evolution of PbI2 and not perovskite by H_2O treatment is a result of the interplay between solvation and hydration of precursor ions. Clancy et al. investigated the solvation of perovskite precursor ions together in different single solvent systems including in DMF. He found that I^- ions passivate Pb^{2+} ions, increasing the solubility of the latter. MA^+ ions also stabilize the PbI_2 complexes, further improving solubility [69]. The inclusion of equimolar DMSO with the precursors is further likely to coordinate with the Pb^{2+} ions much more strongly than I^- ions because of its stronger Lewis basicity than I^-, hence leading to the adduct formation MAI–PbI_2– DMSO.[31] DMF possesses only hydrogen bond acceptor propensity and can most effectively solvate cations. On the other hand, water possess both hydrogen donor and acceptor propensity enabling it to solvate both cations and anions, albeit hydration of cations is weaker than solvation with DMF owing its lower acceptor propensity than DMF (Table 1). H2O forms complexes with DMSO with stronger interaction than DMSO– DMF or water–water interaction.[70,71] Thus, H_2O treatment can attenuate the complexation of Pb^{2+} by withdrawing the availability of DMSO, which will cause a drop in solubility of Pb^{2+}. Hence, PbI_2 is likely to be formed by the addition of H2O as the now poorly solvated Pb^{2+} becomes vulnerable to reaction with I^- ions, which is also poorly hydrated due to its weaker electron density.[72] On the other hand, MA^+ ion remains unavailable because it can form strong solvation shells with DMF as the alkyl hydrogen in its structure can participate in hydrogen bonding with the oxygen atom in DMF.[73] MA^+ is thus likely to be cast-off during spin-coating. Upon annealing, any remaining MA^+ ions will react with H_2O forming MA gas as this reaction can take place at 60 ºC, while precipitated PbI2 undergoes crystal growth.[68,74]

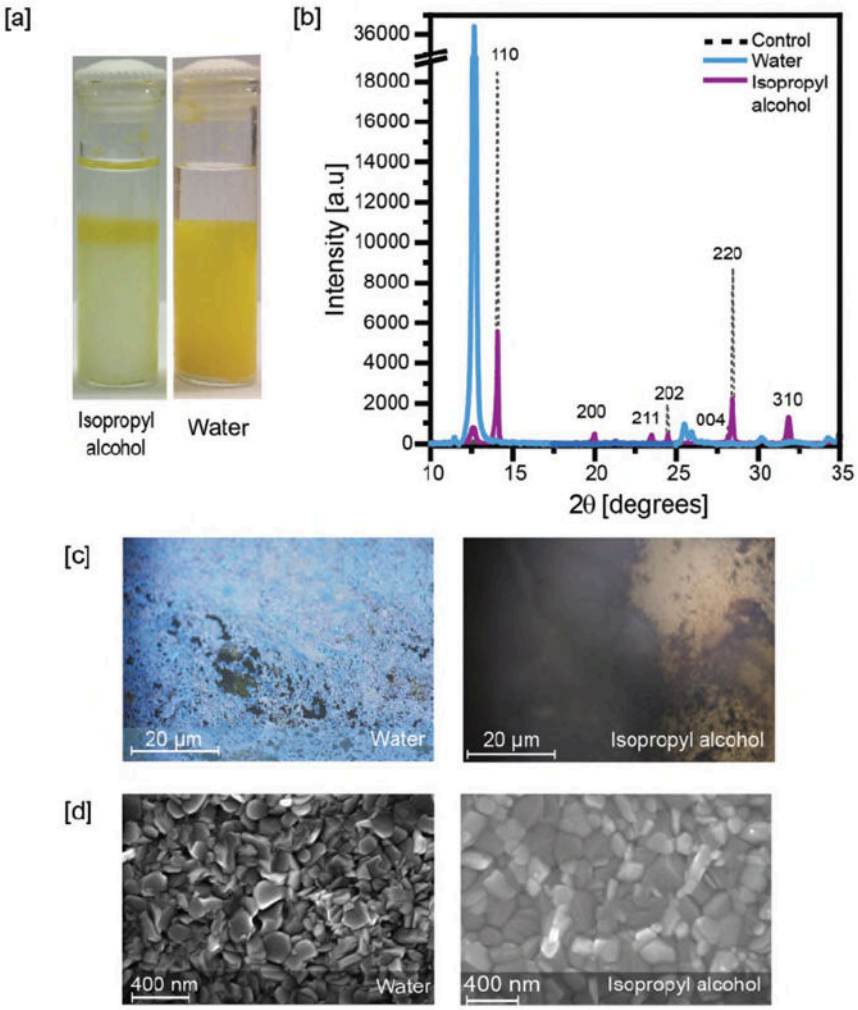

Figure 5. a) Image after precipitation of precursor solution in water and isopropyl alcohol. b) XRD pattern of perovskite films fabricated under ambient environment with water and isopropyl alcohol antisolvents. c) Frames captured during the in situ crystallization imaging of perovskite precursor in water and isopropyl alcohol (Video S2, Supporting Information). d) SEM images of perovskite films fabricated under ambient environment with water and isopropyl alcohol antisolvents.

IPA: IPA is a polar protic, water-miscible solvent. IPA treatment results in uniform and pinhole-free perovskite film formation. However, SEM image show two distinct types of grains in IPA-treated films (Figure 5; Figure S3, Supporting Information). The SEM images are acquired with in-lens detector which can detect differences in work function within a sample with high lateral resolution. An interconnected network of grains in dark gray color is evident in the background, which resemble perovskite grains. In the foreground, a network of brighter, interspersed, plate-like grains are present which resemble PbI_2 grains (Figure S3, Supporting Information). A column of PbI_2 forms on top of the white precipitates in the precipitation experiment, which further confirms IPA treatment leads to formation of PbI_2 (Figure 4a; Video S1, Supporting Information). In the XRD pattern, a strong peak at 12.10□, characteristic signal of (001) plane of PbI_2, is also detected (Figure 5b).

The microstructure of IPA-treated films can be understood from the crystallization mechanism of precursors upon interaction with the antisolvent. Both DMSO and DMF are miscible in IPA. The precipitation experiment shows abrupt precipitation of precursor solution occurs in IPA, which indicates a rapid and higher degree of supersaturation (Video S2, Supporting Information). This leads to a high density of nucleation and thus stronger retardation of crystal growth. The in situ crystallization imaging further provides clear evidence of increased supersaturation, which leads to increased nucleation but reduced crystal growth. A rapid and abrupt termination of crystallization occurs in IPA resulting in uniform and dense but small needle-shaped crystals (Figure 5b; Video S2, Supporting Information). Thus, polar protic IPA causes rapid supersatura-tion, shifting the competition between nucleation versus

crystal growth to favor nucleation and initiating uniform but retarded crystallization. As a result, complete surface coverage with uniform morphology is formed. The integrated peak intensity of (110) plane is greatly reduced in IPA-treated films compared to all other antisolvents treatment, which again suggests stronger retardation of crystal growth. Furthermore, the crystallite size of IPA is 120 nm, the second smallest among the films treated with the different antisolvents, which further confirms retarded crystal growth.

IPA is polar protic and possesses both hydrogen bond acceptor and donor propensities (Table 1). As described for H_2O antisolvent, the hydrogen bond donor propensity is responsible for the formation of PbI2. However, the hydrogen bond donor propensity of IPA is significantly weaker than H_2O. Thus, IPA would lead to reduced formation of PbI_2 than H_2O treatment. A comparison between CB and IPA rules out polarity and surface tension as the parameters dictating the increased nucleation and retarded crystal growth as these parameters are similar in both, yet different crystal growth mechanisms occurs in both. IPA has significantly higher viscosity compared to all other antisolvents including water, which can hinder ion mobility and is likely responsible for increased nucleation and reduced crystal size in IPA.

2.2 Antisolvents in Ambient Versus Inert Environment

To further elucidate the interplay of antisolvent and moisture influence on morphology and crystallinity of the perovskites, and to gauge the effectiveness of borderline polar aprotic solvents for ambient processing, we directly compared morphology and crystallinity of ambient versus inert processing of Tol and CB—the two most popular antisolvents—and PAC. As evident in the SEM morphology images given in **Figure 6**a, Tol- and CB treatment under inert processing environment results in uniform films with full surface coverage, comprising large grains while they form porous films under ambient processing environment. On the other hand, PAC-treated films are compact and uniform under both ambient and inert processing environments. XRD patterns also attest to similar trends as SEM images (Figure S4, Supporting Information). The peak area of the main crystallographic planes (110), (220), and (310) of PAC-treated film remain similar irrespective of the processing environment. By contrast, ambient-processed Tol/ CB-treated films show significant changes in the XRD peak area of one of the main crystallographic peaks compared to their respective inert-processed samples, signifying their susceptibility to processing environment conditions (Figure 6b,c). Additionally, PAC-treated film shows the highest ratio of peak area of (310) with respect to its (110) peak area, which is comparable with the inert-processed Tol- and CB-treated films (Figure 6d). This trend suggests PAC treatment enables highest crystallite growth retardation and crystallite reorientation necessary to induce spherulitic growth. Thus, pinhole-free uniform films are maintained with PAC treatment in both inert and ambient processing environments, whereas Tol- or CB treatment can form uniform films only under inert processing environment.

2.3. Perovskite Solar Cells

To further confirm the efficacy of antisolvent treatment under an ambient environment, PSCs having a planar p–i–n device structure were fabricated in ambient environment (52% RH, 25 ºC) using CB or PAC as antisolvent treatments. The device structure comprised glass/ITO/PEDOT:PSS/$MAPbI_3$/PCBM/ PEIE/Ag. All but the electrodes were solution-processed and only two temperature steps of 140 ºC were employed—which makes the device structure low-cost in comparison to other structures commonly employed for PSCs which embody high cost materials, vacuum-steps, and prolonged high temperature annealing.

Following the trend in the microstructure, PAC treatment led to devices with the highest power conversion efficiency (PCE) of 16.67% with an open-circuit voltage $_{(Voc)}$ of 0.98 V, short-circuit current (J_{sc}): 22.90 mA cm^{-2} and fill factor (FF): 74.26%. Maximum power point tracking showed steady increase initially reaching a stabilized region, which correspond to a PCE of 17.78% (**Figure 7**a,b). The initial increase is attributed to mobile ions which gets depleted upon continuous operation until electrical conductance dominates in the stabilized region, which represents the true efficiency of the device.[75] An integrated photocurrent of 23.4 mA cm^{-2} was calculated from external quantum efficiency measurement (Figure S5, Supporting Information). The slightly lower J_{sc} measured with the solar simulator could be due to spectrum mismatch. To the best of our knowledge, this is the highest efficiency reported for a p–i–n one-step planar device using antisolvents under high humidity ambient condition (above 20% RH). By contrast, the best ambient-processed CB device showed a PCE of 5.56% (Voc: 0.84 V; $_{Jsc:}$ 14.45 mA cm^{-2}, FF: 45.79%). Devices showed reproducible JV characteristics (Table S1 of the Supporting Information contains JV

characteristics under averages and standard deviations and forward and reverse scan directions). The steady-state photoluminescence spectra and UV–vis absorption spectrum of CB and PAC films on glass substrates are also shown in Figure 7c,d, respectively. The emission peak intensity of the PAC-treated film is significantly higher than the CB-treated film, suggesting significantly lower charge recombination in PAC-treated films. Higher FF of PAC-treated devices also reflect the reduced recombination compared to CB-treated films and is a direct result of improved microstructure of PAC-treated films compared to CB-treated films. The UV–vis absorption spectra reveal same bandgap and absorption profile of perovskites processed with PAC- and CB treatment. However, the inert-processed films have slightly higher absorption as well as lower bandgap than their corresponding ambient-processed films. Oxygen and water exposure of perovskite films was recently to shown to shift vacuum-level in perovskites, which might be the cause for reduced absorption in our ambient samples as both processing and annealing were carried out in ambient-conditions.[76] Figure S6 of the Supporting Information contains a box plot depicting the photovoltaic properties of cells processed with different antisolvents.

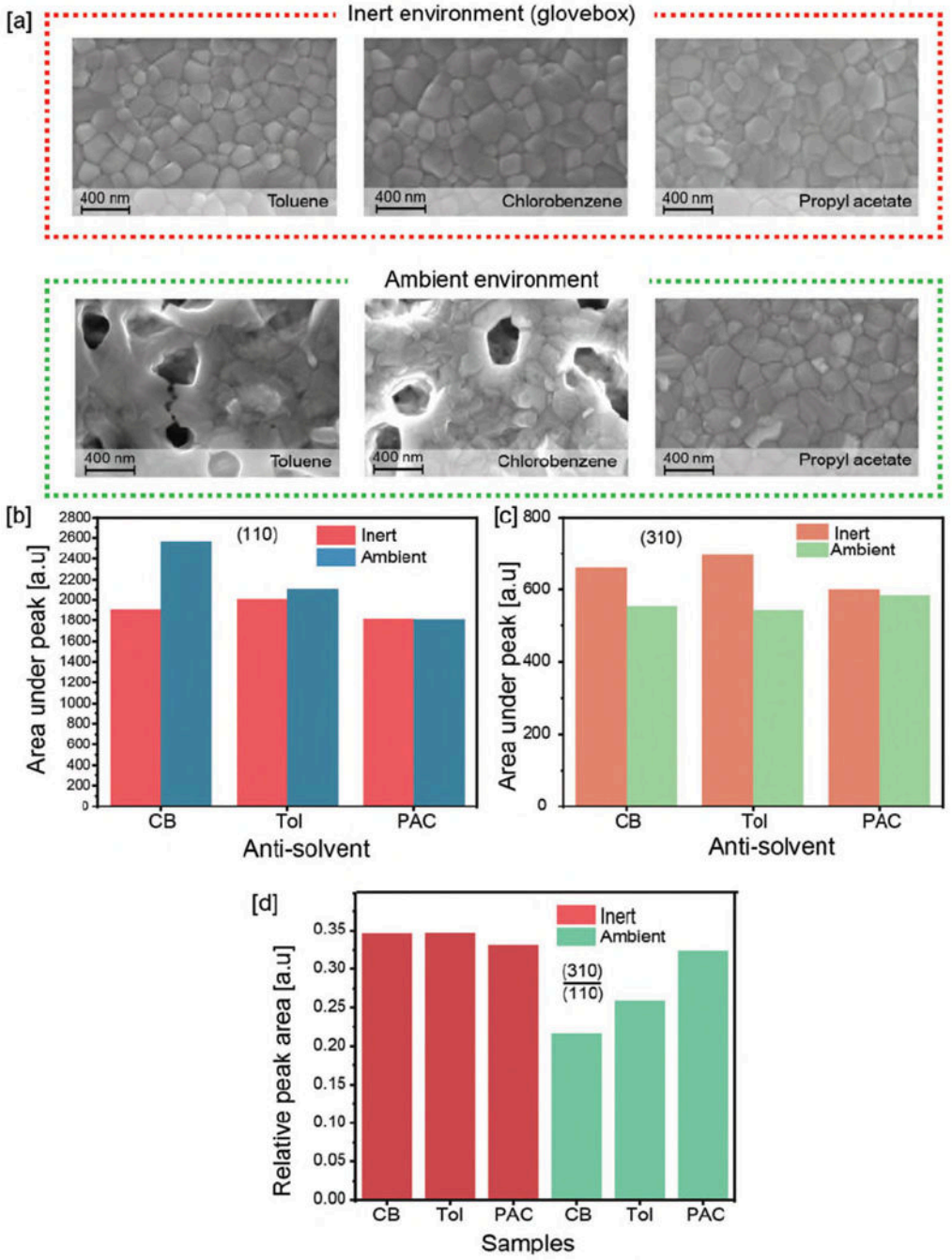

Figure 6. Inert versus ambient-processing. a) SEM images of perovskite films fabricated with different antisolvents—the commonly used toluene (Tol) and chlorobenzene (CB), and propyl acetate (PAC) as investigated in this work, b,c) effect of different antisolvents and processing environment on the evolution of (110) and (310) crystallographic planes of perovskite films, d) effect of different antisolvents and processing environment on the evolution of the (310) plane relative to the (110) plane of the respective perovskite films.

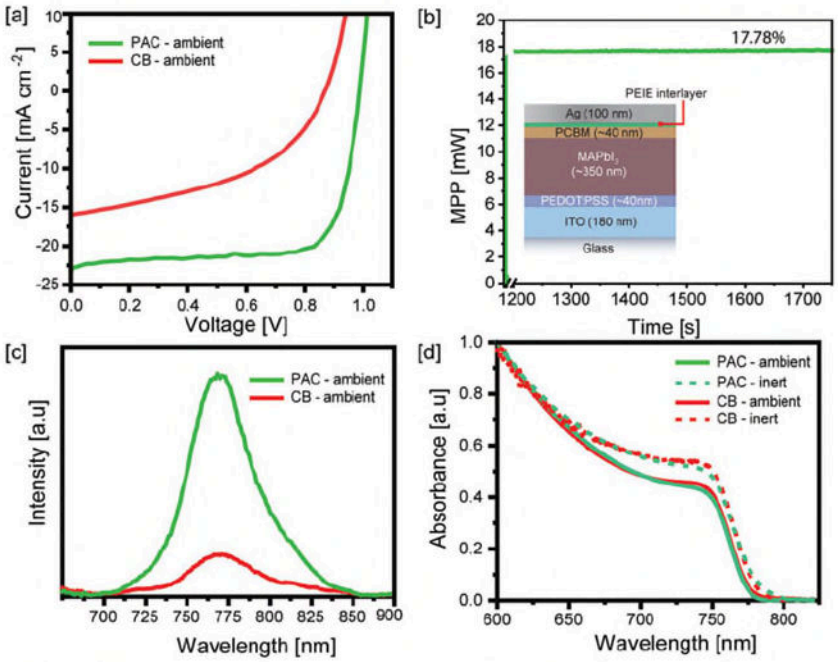

Figure 7. Photovoltaic performance: a) *JV* curve of champion perovskite solar cell fabricated under an ambient environment (25 C, 52% RH) with chlorobenzene (CB) and propyl acetate (PAC) treatment. b) Stabilized efficiency of the best PAC-treated device. c) Photoluminescence response of perovskite films on glass fabricated under ambient environment at an excitation wavelength of 520 nm. d) UV–vis absorption curves of perovskite films prepared under an ambient and inert environment.

3. Conclusion

Perovskites display an inherent tendency toward spherulitic crystallization as crystal growth rate is retarded under inert processing environment using strong Lewis-base additives. In ambient fabrication environment, moisture increases crystal growth rate and induces anisotropies irrespective of the type of solvent additive. Simple precipitation tests and in situ crystallization imaging enabled investigation of microstructure evolution of perovskites, shedding light on to the interplay of antisolvent properties, crystallization, and ambient processing environment. These interactions manifest in the evolution of different crystal habits in different antisolvent. While a slight polarity of the antisolvent induces precipitation, signifying ability to improve the degree of supersaturation during processing, which will encourage nucleation, the hydrogen bonding parameters of antisolvents distinctly impact the nature of crystallization and have direct implications for ambient-processiblity of perovskite films.

Higher hydrogen-bond acceptor propensity of antisol-vent is the dictating parameter conferring resilience toward ambient processing. The nonhydrogen bonding and nonpolar heptane does not affect nucleation/grain growth. The weak hydrogen-bond acceptor polar aprotic solvents such as Tol and CB solvents form an eclectic mix of crystal shapes—sheaves, columns, needles, and spherulites, which manifests as porous films. The strong hydrogen bond accepting polar protic antisol-vents (esters) form a homogenous spherulitic crystallites and lead to uniform films while polar protic solvents that possess both hydrogen-bond donor and acceptor propensities lead to a high density of small but uniform needle-like crystallites, while at the same time, forming PbI_2.

We show that a pinhole-free, uniform perovskite film can be obtained by a high density of homogenous crystallites of any one shape. However, only microstructure preceded by uniform spherulitic crystallization leads to uniform, pinhole-free films with large grains whose crystallographic phases, crystallinity, and crystallite orientations are not drastically affected by the processing environment.

We show that polar aprotic solvents with relatively higher hydrogen-bond acceptor propensity lead to homogenous spher-ulites, which enables humidity-resistant fabrication of PSCs with 17.7% stabilized efficiency in a low-cost p–i–n planar PSCs fabricated in ambient environment with relative humidity over 52%. Moreover, we demonstrate that the simple experiments of precipitation and in situ crystallization can

provide a powerful a priori screening of antisolvents for ambient-resilient processing of PSCs, enabling prediction of morphology and crystallinity required for high efficiency PSCs.

Acknowledgements

D.A. and X.P. contributed equally to this work. Andrew Scully is acknowledged for reviewing this paper. D.A. acknowledges support from CSIRO's OCE Postdoctoral Fellowship, Australian Centre for Advanced Photovoltaics (ACAP) program funded by the Australian Government. X.P. acknowledges the Chinese Government's Fundamental Research Funds for the Central Universities (2016-JL-002).

Keywords
Ambient, crystallization, perovskite, planar, spherulite

References:

[1] Best Research-Cell Efficiencies, NREL, https://www.nrel.gov/pv/ assets/pdfs/best-research-cell-efficiencies (accessed: July 2019).
[2] T. M. Schmidt, T. T. Larsen-Olsen, J. E. Carlé, D. Angmo, F. C. Krebs, *Ad'. Energy Mater.* **2015**, *5*, 1500569.
[3] B. Dou, J. B. Whitaker, K. Bruening, D. T. Moore, L. M. Wheeler, J. Ryter, N. J. Breslin, J. J. Berry, S. M. Garner, F. S. Barnes, S. E. Shaheen, C. J. Tassone, K. Zhu, M. F. A. M. Van Hest, *ACS Energy Lett.* **2018**, *3*, 2558.
[4] Y. Galagan, F. Di Giacomo, H. Gorter, G. Kirchner, I. de Vries, R. Andriessen, P. Groen, *Ad'. Energy Mater.* **2018**, *8*, 1801935.
[5] Y. J. Heo, J. E. Kim, H. Weerasinghe, D. Angmo, T. Qin, K. Sears, K. Hwang, Y. S. Jung, J. Subbiah, D. J. Jones, M. Gao, D. Y. Kim, D. Vak, *Nano Energy* **2017**, *41*, 443.
[6] T. Singh, T. Miyasaka, *Ad'. Energy Mater.* **2018**, *8*, 1700677.
[7] W. Huang, J. S. Manser, P. V. Kamat, S. Ptasinska, *Chem. Mater.* **2016**, *28*, 303.
[8] Q. Tai, P. You, H. Sang, Z. Liu, C. Hu, H. L. W. Chan, F. Yan, *Nat. Commun.* **2016**, *7*, 1.
[9] M. K. Gangishetty, R. W. J. Scott, T. L. Kelly, *Nanoscale* **2016**, *8*, 6300.
[10] G. Sfyri, C. V. Kumar, D. Raptis, V. Dracopoulos, P. Lianos, *Sol. Energy Mater. Sol. Cells* **2015**, *134*, 60.
[11] J. Huang, S. Tan, P. D. Lund, H. Zhou, *Energy En'iron. Sci.* **2017**, *10*, 2284.
[12] Y. Cheng, F. So, S.-W. Tsang, *Mater. Horiz.* **2019**, *6*, 1611.
[13] S. R. Raga, M. C. Jung, M. V. Lee, M. R. Leyden, Y. Kato, Y. Qi, *Chem. Mater.* **2015**, *27*, 1597.
[14] H. Zhou, Q. Chen, G. Li, S. Luo, T.-B. Song, H.-S. Duan, Z. Hong, J. You, Y. Liu, Y. Yang, *Science* **2014**, *345*, 542.
[15] J. You, Z. Hong, T. Bin Song, L. Meng, Y. Liu, C. Jiang, H. Zhou, W. H. Chang, G. Li, Y. Yang, *Appl. Phys. Lett.* **2014**, *105*, 183902.
[16] H. Gao, C. Bao, F. Li, T. Yu, J. Yang, W. Zhu, X. Zhou, G. Fu, Z. Zou, *ACS Appl. Mater. Interfaces* **2015**, *7*, 9110.
[17] Y. Cheng, X. Xu, Y. Xie, H.-W. Li, J. Qing, C. Ma, C.-S. Lee, F. So, S.-W. Tsang, *Sol. RRL* **2017**, *1*, 1770131.
[18] H. S. Ko, J. W. Lee, N. G. Park, *J. Mater. Chem. A* **2015**, *3*, 8808.
[19] X. Xu, M. Li, Y.-M. Xie, Y. Ma, C. Ma, Y. Cheng, S.-W. T. Chun-Sing Lee, *ACS Appl. Mater. Interfaces* **2019**, *11*, 6126.
[20] M. Saliba, T. Matsui, K. Domanski, J.-Y. Seo, A. Ummadisingu, S. M. Zakeeruddin, J.-P. Correa-Baena, W. R. Tress, A. Abate, A. Hagfeldt, M. Gratzel, *Science* **2016**, *354*, 206.
[21] M. Saliba, T. Matsui, J.-Y. Seo, K. Domanski, J.-P. Correa-Baena, M. K. Nazeeruddin, S. M. Zakeeruddin, W. Tress, A. Abate, A. Hagfeldt, M. Grätzel, *Energy En'iron. Sci.* **2016**, *9*, 1989.
[22] J. Troughton, K. Hooper, T. M. Watson, *Nano Energy* **2017**, *39*, 60.
[23] M. Li, Y. M. Xie, X. Xu, Y. Huo, S. W. Tsang, Q. D. Yang, Y. Cheng, *Org. Electron.* **2018**, *63*, 159.
[24] X. Liu, J. He, P. Wang, Y. Liu, J. Xiao, Z. Ku, Y. Peng, F. Huang, Y. B. Cheng, J. Zhong, *ChemSusChem* **2019**, *12*, 2385.

[25] A. A. Thorat, S. V. Dalvi, *Chem. Eng. J.* **2012**, *181–182*, 1.
[26] Y. Lan, M. G. Corradini, X. Liu, T. E. May, F. Borondics, R. G. Weiss, M. A. Rogers, *Langmuir* **2014**, *30*, 14128.
[27] F. Huang, Y. Dkhissi, W. Huang, M. Xiao, I. Benesperi, S. Rubanov, Y. Zhu, X. Lin, L. Jiang, Y. Zhou, *Nano Energy* **2014**, *10*, 10.
[28] M. Xiao, F. Huang, W. Huang, Y. Dkhissi, Y. Zhu, J. Etheridge, A. Gray-Weale, U. Bach, Y. Cheng, L. Spiccia, *Angew. Chem.* **2014**, *126*, 10056.
[29] D. Zhao, Y. Yu, C. Wang, W. Liao, N. Shrestha, C. R. Grice, A. J. Cimaroli, L. Guan, R. J. Ellingson, K. Zhu, X. Zhao, R.-G. Xiong, Y. Yan, *Nat. Energy* **2017**, *2*, 17018.
[30] D. Bi, C. Yi, J. Luo, J.-D. Décoppet, F. Zhang, S. M. Zakeeruddin, X. Li, A. Hagfeldt, M. Grätzel, *Nat. Energy* **2016**, *1*, 16142.
[31] N. Ahn, D. Y. Son, I. H. Jang, S. M. Kang, M. Choi, N. G. Park, *J. Am. Chem. Soc.* **2015**, *137*, 8696.
[32] S. Tang, Y. Deng, X. Zheng, Y. Bai, Y. Fang, Q. Dong, H. Wei, J. Huang, *Ad'. Energy Mater.* **2017**, *7*, 1700302.
[33] W. Nie, H. Tsai, R. Asadpour, J.-C. Blancon, A. J. Neukirch, G. Gupta, J. J. Crochet, M. Chhowalla, S. Tretiak, M. A. Alam, H.-L. Wang, A. D. Mohite, *Science* **2015**, *347*, 522.
[34] G. E. Eperon, S. D. Stranks, C. Menelaou, M. B. Johnston, L. M. Herz, H. J. Snaith, *Energy En'iron. Sci.* **2014**, *7*, 982.
[35] F. Wang, T. Zhang, Y. Wang, D. Liu, P. Zhang, H. Chen, L. Ji, L. Chen, Z. D. Chen, J. Wu, X. Liu, Y. Li, S. Li, *J. Mater. Chem. A* **2019**, *7*, 12166.
[36] N. J. Jeon, J. H. Noh, Y. C. Kim, W. S. Yang, S. Ryu, S. Il Seok, *Nat. Mater.* **2014**, *13*, 897.
[37] S. Paek, P. Schouwink, E. N. Athanasopoulou, K. T. Cho, G. Grancini, Y. Lee, Y. Zhang, F. Stellacci, M. K. Nazeeruddin, P. Gao, *Chem. Mater.* **2017**, *29*, 3490.
[38] Y. Wu, A. Islam, X. Yang, C. Qin, J. Liu, K. Zhang, W. Peng, L. Han, *Energy En'iron. Sci.* **2014**, *7*, 2934.
[39] M. Jung, S. G. Ji, G. Kim, S. Il Seok, *Chem. Soc. Re'.* **2019**, *48*, 2011.
[40] S. Rahimnejad, A. Kovalenko, S. M. Forés, C. Aranda, A. Guerrero, *ChemPhysChem* **2016**, *17*, 2795.
[41] L. Gránásy, T. Pusztai, T. Börzsönyi, J. A. Warren, J. F. Douglas, *Nat. Mater.* **2004**, *3*, 645.
[42] J. Li, R. Munir, Y. Fan, T. Niu, Y. Liu, Y. Zhong, Z. Yang, Y. Tian, B. Liu, J. Sun, D. M. Smilgies, S. Thoroddsen, A. Amassian, K. Zhao, S. (Frank) Liu, *Joule* **2018**, *2*, 1313.
[43] Z. Bi, X. Rodriguez-Martinez, C. Aranda, E. Pascual-San-Jose, A. R. Goñi, M. Campoy-Quiles, X. Xu, A. Guerrero, *J. Mater. Chem. A* **2018**, *6*, 19085.
[44] W. Li, J. Fan, J. Li, Y. Mai, L. Wang, *J. Am. Chem. Soc.* **2015**, *137*, 10399.
[45] M. Hiroshi, N. Yoshinaho, N. Miharu, *Chem. Lett.* **1980**, *9*, 663.
[46] A. Chand, S. Chowdhuri, *J. Chem. Sci.* **2016**, *128*, 991.
[47] J. T. Cabral, A. Luzar, J. Teixeira, M. C. Bellissent-Funel, *J. Chem. Phys.* **2000**, *113*, 8736.
[48] N. S. Venkataramanan, *J. Mol. Model.* **2016**, *22*, 151.
[49] D. D. Macdonald, D. Dunay, G. Hanlon, J. B. Hyne, *Can. J. Chem. Eng.* **1971**, *49*, 420.
[50] I. E. Maloka, S. Y. Ibrahim, *Pet. Sci. Technol.* **2004**, *22*, 1571.
[51] K. Wang, Z. Jin, L. Liang, H. Bian, D. Bai, H. Wang, J. Zhang, Q. Wang, L. Shengzhong, *Nat. Commun.* **2018**, *9*, 4544.
[52] K. L. Svane, A. C. Forse, C. P. Grey, G. Kieslich, A. K. Cheetham, A. Walsh, K. T. Butler, *J. Phys. Chem. Lett.* **2017**, *8*, 6154.
[53] W. S. Yang, N. J. J. Jun Hong Noh, Y. C. Kim, S. Ryu, J. Seo, S. Il Seok, *Science* **2015**, *348*, 2013.
[54] J. S. Manser, M. I. Saidaminov, J. A. Christians, O. M. Bakr, P. V. Kamat, *Acc. Chem. Res.* **2016**, *49*, 330.
[55] L. Contreras-Bernal, C. Aranda, M. Valles-Pelarda, T. T. Ngo, S. Ramos-Terrón, J. J. Gallardo, J. Navas, A. Guerrero, I. Mora-Seró, J. Idigoras, J. A. Anta, *J. Phys. Chem. C* **2018**, *122*, 5341.
[56] P. Winget, D. M. Dolney, D. J. Giesen, C. J. Cramer, D. G. Truhlar, Minnesota Solvent Descriptor Database, http://comp.chem.umn. edu/solvation/mnsddb.pdf, **2010** (accessed: December 2018).
[57] Y. Marcus, *Chem. Soc. Rev.* **1993**, *22*, 409.
[58] M. H. Abraham, *J. Phys. Org. Chem.* **1993**, *6*, 660.
[59] C. H. Gu, H. Li, R. B. Gandhi, K. Raghavan, *Int. J. Pharm.* **2004**, *283*, 117.

[60] M. M. Lee, J. Teuscher, T. Miyasaka, T. N. Murakami, H. J. Snaith, *Science* **2012**, *338*, 643.
[61] P. Docampo, F. C. Hanusch, N. Giesbrecht, P. Angloher, A. Ivanova, T. Bein, *APL Mater.* **2014**, *2*, 081508.
[62] J. A. Koza, J. C. Hill, A. C. Demster, J. A. Switzer, *Chem. Mater.* **2016**, *28*, 399.
[63] R. Bjørk, V. Tikare, H. L. Frandsen, N. Pryds, *J. Am. Ceram. Soc.* **2013**, *96*, 103.
[64] A. A. Zhumekenov, V. M. Burlakov, M. I. Saidaminov, A. Alofi, M. A. Haque, B. Turedi, B. Davaasuren, I. Dursun, N. Cho, A. M. El-Zohry, *ACS Energy Lett.* **2017**, *2*, 1782.
[65] L. Gránásy, T. Pusztai, G. Tegze, J. A. Warren, J. F. Douglas, *Phys. Rev. E* **2005**, *72*, 011605.
[66] R. Beck, J. P. Andreassen, *Cryst. Growth Des.* **2010**, *10*, 2934.
[67] E. Ozden-Yenigun, E. Simsek, Y. Z. Menceloglu, C. Atilgan, *Phys. Chem. Chem. Phys.* **2013**, *15*, 17862.
[68] Z. Zheng, S. Wang, D. Li, A. Liu, B. Huang, H. Zhao, L. Zhang, *J. Cryst. Growth* **2007**, *308*, 398.
[69] J. Stevenson, B. Sorenson, V. H. Subramaniam, J. Raiford, P. P. Khlyabich, Y. Loo, P. Clancy, *Chem. Mater.* **2017**, *29*, 2435.
[70] K. I. Oh, C. R. Baiz, *J. Phys. Chem. B* **2018**, *122*, 5984.
[71] O. A. El Seoud, *Pure Appl. Chem.* **2007**, *79*, 1135.
[72] I. Persson, K. Lyczko, D. Lundberg, L. Eriksson, P. Anna, *Inorg. Chem.* **2011**, *50*, 1058.
[73] M. V. Fedotova, S. E. Kruchinin, *Russ. Chem. Bull.* **2012**, *61*, 240.
[74] B. Brunetti, C. Cavallo, A. Ciccioli, G. Gigli, A. Latini, *Sci. Rep.* **2016**, *6*, 31896.
[75] Y. C. Zhao, W. K. Zhou, X. Zhou, K. H. Liu, D. P. Yu, Q. Zhao, *Light: Sci. Appl.* **2017**, *6*, e16243.
[76] J. Yang, Z. Yuan, X. Liu, S. Braun, Y. Li, J. Tang, F. Gao, C. Duan, M. Fahlman, Q. Bao, *ACS Appl. Mater. Interfaces* **2018**, *10*, 16225.